Journal of Computational Physics 228 (2009) 1639–1657

Contents lists available at ScienceDirect

Journal of Computational Physics

journal homepage: www.elsevier.com/locate/jcp

Direct numerical simulation of scalar transport using unstructured finite-volume schemes

Riccardo Rossi *

Laboratorio di Termofluidodinamica Computazionale, Seconda Facoltà di Ingegneria di Forlì, Università di Bologna, Via Fontanelle 40, 47100 Forlì, Italy

ARTICLE INFO

Article history:
Received 25 June 2008
Received in revised form 28 September 2008
Accepted 3 November 2008
Available online 11 November 2008

Keywords:
Scalar transport
High-fidelity simulations
Finite-volume schemes
Unstructured grids
Central interpolation operators

ABSTRACT

An unstructured finite-volume method for direct and large-eddy simulations of scalar transport in complex geometries is presented and investigated. The numerical technique is based on a three-level fully implicit time advancement scheme and central spatial interpolation operators. The scalar variable at cell faces is obtained by a symmetric central interpolation scheme, which is formally first-order accurate, or by further employing a high-order correction term which leads to formal second-order accuracy irrespective of the underlying grid. In this framework, *deferred-correction* and *slope-limiter* techniques are introduced in order to avoid numerical instabilities in the resulting algebraic transport equation. The accuracy and robustness of the code are initially evaluated by means of basic numerical experiments where the flow field is assigned *a priori*. A direct numerical simulation of turbulent scalar transport in a channel flow is finally performed to validate the numerical technique against a numerical dataset established by a spectral method. In spite of the linear character of the scalar transport equation, the computed statistics and spectra of the scalar field are found to be significantly affected by the spectral-properties of interpolation schemes. Although the results show an improved spectral-resolution and greater spatial-accuracy for the high-order operator in the analysis of basic scalar transport problems, the low-order central scheme is found superior for high-fidelity simulations of turbulent scalar transport.

1. Introduction

In the development of numerical techniques for computational fluid dynamics, the finite-volume method has been mainly adopted in the analysis of practical flows because of the low effort required to derive robust numerical schemes for complex geometries. On the other hand, direct numerical simulations (DNS) and large-eddy simulations (LES) of turbulence have been historically based on spectral and finite difference methods [1], which provide outstanding accuracy and computational efficiency in regular domains. However, the last decade has shown a growing interest toward the finite-volume method for the numerical simulation of turbulence outside the context of Reynolds averaged Navier–Stokes (RANS) computations. This interest has been mainly driven by large-eddy simulations of turbulent flows in complex geometries, leading to a strong research effort in the development of suitable numerical schemes [2–4]. The increasing availability of computational resources and the recent improvements of numerical methods have made it feasible to perform LES computations in complex industrial geometries at moderate Reynolds numbers [5].

The main advantage of the finite-volume method is the conservative form of the governing equations being solved, which leads to good conservation properties of primitive flow variables for the resulting numerical scheme. Although this property

* Tel.: +39 0543 374457; fax: +39 0543 374477.
E-mail address: riccardo.rossi12@unibo.it

0021-9991/$ - see front matter © 2008 Elsevier Inc. All rights reserved.
doi:10.1016/j.jcp.2008.11.001

is of primary importance, the work of Mahesh et al. [4] showed that second-order statistical moments, like the kinetic energy, must be conserved as well in order to obtain reliable finite-volume schemes for high-fidelity simulations of turbulence. The analysis of Felten and Lund [6] has recently shown that for co-located schemes the main sources of error in second-order conservation for co-located schemes are due to the momentum interpolation practice, originally introduced by Rhie and Chow [7], and convection interpolation operators. The same authors carried out numerical experiments of a turbulent channel flow using LES showing that such numerical errors are not a serious issue when reasonable fine grids and small time steps are required. Further successful analysis of co-located finite-volume schemes can be found in Benhamadouche et al. [8] and in the work of Silva Lopes and Palma [9], where the influence of a non-orthogonal grid system has also been investigated.

In spite of the great research effort toward the momentum equation and the pressure–velocity coupling, less attention has been dedicated to direct and large-eddy simulations of scalar transport in complex geometries. However, it must be noted that physical bounds to computed scalar values, like species concentration or temperature, and the absence of the continuity constraint yield greater difficulties from the viewpoint of numerical stability [10,11]. Examples of direct numerical simulations of turbulent scalar transport using finite-volume schemes can be found in Piller and Nobile [12], Piller et al. [13] and Stalio and Nobile [14], but the computations were limited to structured grids. In order to approach high-fidelity simulations of scalar transport in complex geometries, an unstructured finite-volume scheme for arbitrary grids is presented and investigated in this paper. In the case of the scalar transport equation, provided that mass fluxes satisfy the continuity constraint, the most critical numerical issue reduces to the construction of reliable convection interpolation operators. Although central interpolations have been established as reliable operators for accurate predictions of turbulent flows, the basic symmetric form of central schemes leads to second-order accuracy only for orthogonal meshes with constant spacing, being first-order accurate when the mesh is characterized by a displacement between the face center and the midpoint of the line connecting the cell-centroids [3]. While this limitation is less restrictive in the case of free-shear flows (e.g. wakes and jets), the numerical simulation of wall-bounded turbulence can be largely affected by the basic low-order central interpolation. Therefore, the present work is focused to a first comparative study of the symmetric central scheme and a high-order central interpolation designed to provide second-order accuracy irrespectively of the underlying grid. Note that advection schemes for scalar transport have been also evaluated by Châtelain et al. [15] in the framework of LES. However, the basic central symmetric operator and high-order correction terms suitable to arbitrary grids have not been considered in the analysis.

The numerical scheme is based on a cell-centered second-order accurate finite-volume method. Time advancement is performed by a fully implicit second-order accurate three-level scheme, while the spatial discretization of diffusive terms is based on a second-order central difference method, which also accounts for cross-diffusion corrections in regions where the grid is not orthogonal. The scalar variable at cell faces is obtained employing the standard low-order central scheme and the high-resolution central scheme originally introduced in the work of Batten et al. [16] for the unstructured elements method. The deferred-correction technique [17] is finally adopted to improve the stability of advection schemes. An initial evaluation of accuracy and spectral properties of interpolation operators is carried out by solving the scalar transport equation over a two-dimensional domain where the flow field is assumed to be known *a priori*. A direct numerical simulation of turbulent scalar transport in a flat channel is finally performed in order to validate the present code and to further compare the convection interpolation operators against available datasets established by a spectral method.

The paper is organized as follows. In Section 2 the numerical technique employed to solve the scalar transport equation is introduced along with a detailed analysis of adopted interpolation operators. The basic numerical experiments performed to investigate the overall accuracy of the numerical method and the basic properties of the low and high-order central interpolation are presented in Section 3, while the direct numerical simulation of turbulent scalar transport in the flat channel is presented in Section 4. Concluding remarks are finally summarized in Section 5.

2. Numerical technique

The transport equation for a generic scalar variable can be written in the following form:

$$\frac{\partial \phi}{\partial t} + \frac{\partial}{\partial x_j}(u_j \phi) = \Gamma \frac{\partial^2 \phi}{\partial x_j \partial x_j} + P_\phi - D_\phi, \tag{1}$$

where the scalar rate of change and the advective transport performed by the flow field are placed on the left-hand side and a molecular transport based on a constant diffusivity coefficient Γ is assumed on the right-hand side. The last two terms finally account for processes of scalar production and dissipation. Eq. (1) can be integrated over a control volume leading to the integral form of the scalar transport equation

$$\int_V \frac{\partial \phi}{\partial t} dV + \int_S (u_j \phi) n_j dS = \int_S \Gamma \frac{\partial \phi}{\partial x_j} n_j dS + \int_V (P_\phi - D_\phi) dV, \tag{2}$$

where n_j is the surface normal unit vector pointing outward from the control volume and the Green–Gauss formula is used to obtain the surface integral form of transport terms.

The numerical method employed to solve the scalar transport equation (2) is based on a second order-accurate finite-volume scheme. In order to employ the code to predict the turbulent scalar transport in complex geometries, an unstructured

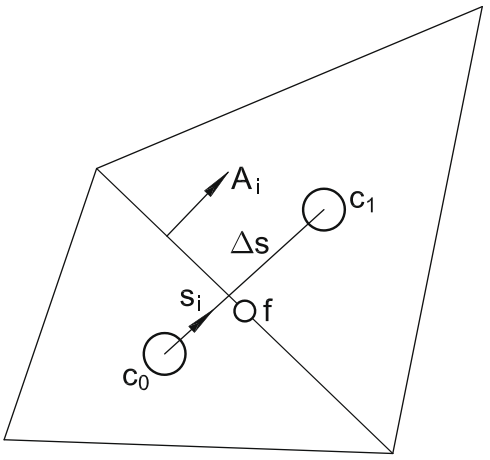

Fig. 1. Grid connectivity and geometrical definitions.

grid connectivity is adopted and scalar fluxes are reconstructed using the face-based data structure shown in Fig. 1, where c_0 and c_1 denote the cell-centroids sharing the same face of the computational grid and f is the face centroid. Note that the same definitions apply also to quadrilateral and hexahedral cells employed in the computations. The scalar variable is located at the cell centroid and both surface and volume integrals are numerically estimated using the midpoint rule, leading to formal second-order accuracy in space. Time advancement is performed by a second-order accurate three-level scheme [18] where both the diffusive and advective terms are treated implicitly in order to avoid the more stringent restriction of the computational time step which follows by adopting semi-implicit schemes [19]. The resulting semi-discrete scalar transport equation reads as follows:

$$\frac{3\phi^{n+1}-4\phi^{n}+\phi^{n-1}}{2\Delta t}\Delta V+\sum_{f}u_{j}^{n+1}\phi_{f}^{n+1}A_{j}=\sum_{f}\Gamma\frac{\partial\phi^{n+1}}{\partial x_{j}}\bigg|_{f}A_{i}+S_{\phi}\Delta V, \tag{3}$$

where Δt and ΔV are the time-step size and the cell volume respectively, A_j is the face area vector and u_j^{n+1} is the face velocity available from the solution of the momentum equation, which must satisfy the continuity constraint. It is stressed that the summations in Eq. (3) require the estimation of the scalar fluxes at the face centroid over all faces of the control volume in order to keep second-order accuracy, while the volume integrals involved in the first and the last terms of the semi-discrete transport equation implicitly satisfy the midpoint rule since the scalar variable is located at cell-centroids.

2.1. Convection interpolation operators

The interpolation operators employed to evaluate the scalar variable at cell faces ϕ_f are based on the following high-resolution central scheme originally introduced in the work of Batten et al. [16]

$$\phi_{f}=\frac{1}{2}(\phi_{0}+\phi_{1})+\frac{1}{2}\left(\frac{\partial\phi}{\partial x_{i}}\bigg|_{0}R_{0i}+\frac{\partial\phi}{\partial x_{i}}\bigg|_{1}R_{1i}\right), \tag{4}$$

where R_{ki} is the displacement vector between the center of the generic neighboring cell c_k and the face centroid, as shown in Fig. 2. As it can be noted from Eq. (4), the interpolation scheme is obtained from the sum of two basic terms. The first one is given by a symmetric averaging of scalar values from neighboring cells, leading to a low-order central interpolation (LO-CD) which is formally first-order accurate over arbitrary grids. Nonetheless, several researchers [2,4–6] have shown that the LO-CD scheme is able to conserve second-order moments and it has been successfully employed for the solution of the Navier-Stokes equations in complex geometries using LES. The high-order central interpolation (HO-CD) is obtained by adding to the LO-CD scheme the correction operator on the right-hand side of Eq. (4), based on cell-centered scalar gradients in neighboring cells c_0 and c_1, leading to a formally second-order accurate interpolation irrespectively of the underlying computational grid. In the present code cell-centered scalar gradients are evaluated through the Green–Gauss formula

$$\frac{\partial\phi}{\partial x_{i}}\approx\sum_{f}\phi_{f}A_{i}, \tag{5}$$

where the scalar value at the face centroid is evaluated using the standard symmetric central scheme irrespectively of the grid geometry. Note that although more elaborate gradient approximations (like node-based or least-squares methods) can be adopted, the resulting effect on the high-order central interpolation has not been considered in the present work.

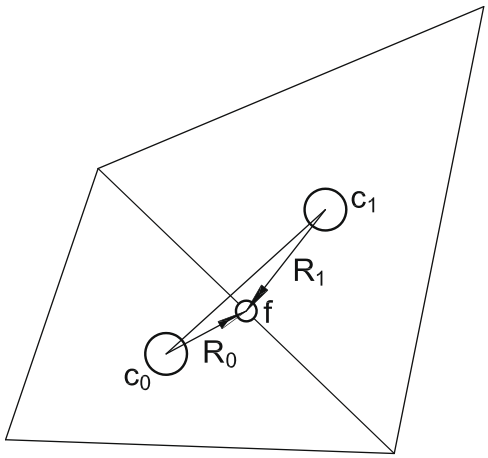

Fig. 2. Geometrical definitions for convection interpolation operators.

A similar expression to the central scheme (4) has been introduced by Felten and Lund [6] to study the effect of high-order corrections to the LO-CD scheme for the solution of the momentum equation. However, the correction term was limited to a weighting factor based on the mutual distance between the center of the neighboring cells and the face centroid. Therefore, the interpolation accounted for non-uniform mesh spacing only. Kim and Choi [3] have shown that a distance-weighted operator is not able to give second-order accuracy over unstructured meshes. They were successful to achieve second-order accuracy by adopting a correction term based on the scalar gradient at the cell-face. The face-based gradient was estimated using the interpolated values at the nodes of the face, but this technique is limited to two-dimensional computations. Therefore, in the present code the correction term employed in the central interpolation operator is introduced on a cell-centered basis in order to allow the extension to three-dimensional models without further effort.

The basic properties of the low and high-order central operators can be investigated by considering the uniformly-spaced one-dimensional grid shown in Fig. 3. Although the numerical experiments are directly extended to higher dimensions, the analysis will be helpful to examine the results presented in Sections 3 and 4. Let j denote the position of the cell centroid. If the cell face is located at $j+\frac{1}{2}$, Taylor expansion analysis gives the following expression of truncation error for the low and the high-order scheme, respectively

$$\phi_{j+\frac{1}{2}}^{\mathrm{LO-CD}} = \frac{(\phi_{j+1}+\phi_j)}{2} - \left.\frac{\partial^2\phi}{\partial x^2}\right|_j \frac{\Delta x^2}{8} - \left.\frac{\partial^3\phi}{\partial x^3}\right|_j \frac{\Delta x^3}{16} + O(\Delta x^4), \tag{6}$$

$$\phi_{j+\frac{1}{2}}^{\mathrm{HO-CD}} = \frac{(-\phi_{j-1}+5\phi_j+5\phi_{j+1}+\phi_{j+2})}{8} + \left(\left.\frac{\partial^2\phi}{\partial x^2}\right|_j + \left.\frac{\partial^2\phi}{\partial x^2}\right|_{j+1}\right)\frac{\Delta x^2}{16} + \left(\left.\frac{\partial^3\phi}{\partial x^3}\right|_j - \left.\frac{\partial^3\phi}{\partial x^3}\right|_{j+1}\right)\frac{\Delta x^3}{32} + O(\Delta x^4), \tag{7}$$

where Δx is the cell size. Note that the Green–Gauss scheme (5) reduces in this case to the standard central-difference operator

$$\left.\frac{\partial\phi}{\partial x}\right|_j = \frac{\phi_{j+1}-\phi_{j-1}}{2\Delta x} - \frac{1}{6}\left.\frac{\partial^3\phi}{\partial x^3}\right|_j \Delta x^2 + O(\Delta x^3). \tag{8}$$

Eqs. (6) and (7) show that the magnitude of truncation errors over regular grids is similar for the low and high-order interpolation operators. However, for the HO-CD scheme the error is given by the sum of scalar gradients at both sides of cell faces, the odd terms having an opposite sign.

In the framework of direct and large-eddy simulations of scalar transport, an additional crucial characteristic of interpolation operators is the so-called *spectral-resolution*, i.e. the ability of the scheme to resolve wave-like motions of several lengthscales. The spectral resolution for a given scheme can be investigated through the Fourier analysis of the numerical error. If the scalar variable is assumed periodic over the numerical stencil $[-L/2, L/2]$ composed of N discrete volumes of size $\Delta x = L/N$, the Fourier expansion of $\phi(x)$ is given by

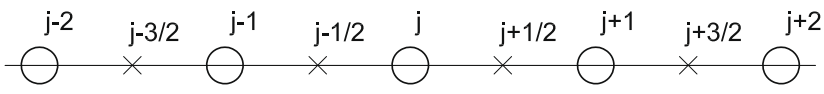

Fig. 3. Sketch of one-dimensional finite-volume grid: (○) cell-centroid location, (×) cell-face location.

$$\phi = \sum_{k=0}^{N/2} \hat{\phi}_k e^{i\alpha x^+}, \tag{9}$$

while the first derivative is

$$\frac{\partial \phi}{\partial x^+} = \sum_{k=0}^{N/2} i\alpha \hat{\phi}_k e^{i\alpha x^+}, \tag{10}$$

where $\alpha = 2\pi k \Delta x / L$ and $x^+ = x/\Delta x$ denote a scaled wavenumber and a scaled coordinate, respectively. Introducing the expansion (9) into a generic interpolation operator gives

$$\phi = \sum_{k=0}^{N/2} \hat{\phi}_k^* e^{i\alpha x^+}, \tag{11}$$

where $\hat{\phi}_k^*$ are the modified Fourier coefficients given by the numerical approximation. The spectral-resolution of the interpolation scheme is thus evaluated through the following transfer function

$$H(\alpha) = \frac{\hat{\phi}_k^*}{\hat{\phi}_k}. \tag{12}$$

For the one-dimensional form of low and high-order interpolation operators (6) and (7) the transfer functions are

$$H_{\mathrm{LO-CD}} = \cos\left(\frac{1}{2}\alpha\right), \tag{13}$$

$$H_{\mathrm{HO-CD}} = \frac{5}{4}\cos\left(\frac{1}{2}\alpha\right) - \frac{1}{4}\cos\left(\frac{3}{2}\alpha\right). \tag{14}$$

The profiles of transfer functions (13) and (14) versus the wavenumber in Fig. 4 shows an improved spectral-resolution for the HO-CD operator compared to the LO-CD scheme. A final insight on spectral properties of discretization schemes is given by the modified wavenumber analysis, which highlights the dissipative or dispersive effect of truncation errors over the Fourier modes. In the analysis of interpolation operators, the modified wavenumber is obtained by estimating the first derivative of the scalar variable through interpolated face values (Ham, personal communication) as follows

$$\left.\frac{\partial \phi}{\partial x}\right|_j \approx \frac{\phi_{j+\frac{1}{2}} - \phi_{j-\frac{1}{2}}}{\Delta x}. \tag{15}$$

Using again the expansion (9) to evaluate the interpolated face values and then substituting in Eq. (15) yields for the generic interpolation scheme

$$\frac{\partial \phi}{\partial x^+} = \sum_{k=0}^{N/2} i\alpha^* \hat{\phi}_k e^{i\alpha x^+}, \tag{16}$$

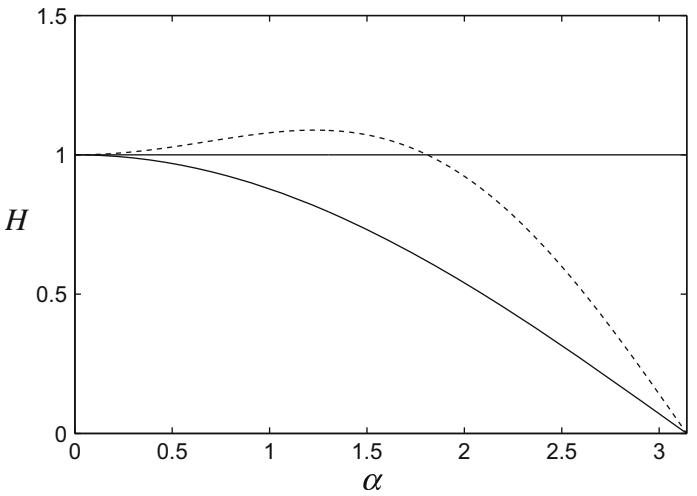

Fig. 4. Transfer function of convection interpolation operators: (—) LO-CD operator, (– – –) HO-CD operator; the thick solid line shows the ideal profile $H = 1$.

which gives the definition of the modified wavenumber α^*. For the low and high-order interpolation operators (6) and (7) the expression of the modified wavenumber is

$$\alpha^*_{\mathrm{LO-CD}} = \sin(\alpha), \tag{17}$$

$$\alpha^*_{\mathrm{HO-CD}} = \frac{3}{2}\sin(\alpha) - \frac{1}{4}\sin(2\alpha). \tag{18}$$

Eqs. (17) and (18) show that for both interpolation operators the modified wavenumber is imaginary, leading to a dissipation-free discretization over regular grids. However, note that this is not the case of the HO-CD scheme when employed over arbitray grids, owing to the high-order correction term in Eq. (4) which may lead to asymmetric interpolations. The amount of numerical dispersion given by the two central interpolation operators is examined in Fig. 5, where the modified wavenumbers (17) and (18) are presented along with the profile for a compact fourth-order scheme. As expected, numerical dispersion is minimized by the HO-CD scheme, which is close to the reference compact scheme in the range $\left[0, \frac{\pi}{2}\right]$. It is also worth noting that within the same interval the modified wavenumber for the high-order scheme falls slightly above the exact profile, indicating a faster numerical phase speed compared to the real phase speed. Note that a similar result has been also reported by Li [20] in the analysis of upwind-biased schemes.

2.1.1. Slope-limiter technique

The adoption of central schemes for advection discretization leads to severe stability limits owing to the dispersive nature of the numerical error. In order to improve the robustness of the present code, both central interpolation operators are introduced in the discrete scalar transport equation with the help of the *deferred-correction* technique of Koshla and Rubin [17], which has proven to notably relax the stability limit associated with central discretization schemes. However, when the high-order correction term is employed in the interpolation operator (4) another source of numerical instability may rise in the form of unbounded reconstructed face values. Therefore, the *slope-limiter* technique, originally introduced in the work of Van Leer [21] on hyperbolic conservation laws, is adopted when the high-order central scheme is employed in direct numerical simulation of scalar transport.

The HO-CD operator (4) is obtained through the linear reconstruction at both sides of cell faces given by

$$\phi(x,y) = \phi(x_0,y_0) + \left.\frac{\partial\phi}{\partial x_i}\right|_0 R_i, \tag{19}$$

where R_i is the displacement vector between the cell centroid c_0 and any point within the cell volume. In the framework of unstructured finite-volume schemes, the work of Barth and Jespersen [22] has shown that stable reconstructions of face values of the type (19) are obtained by limiting the magnitude of the gradient as follows:

$$\left.\frac{\partial\phi}{\partial x_i}\right|_{0,L} = \alpha \left.\frac{\partial\phi}{\partial x_i}\right|_0, \tag{20}$$

where L denotes the limited gradient and α is the so-called slope-limiter. The slope limiter is defined in such a way that reconstructed values at cell faces do not exceed the extrema of suitable neighboring values. Using different definitions for the local extrema, it is possible to develop different types of limiters. The limiter introduced by Barth & Jespersen is adopted

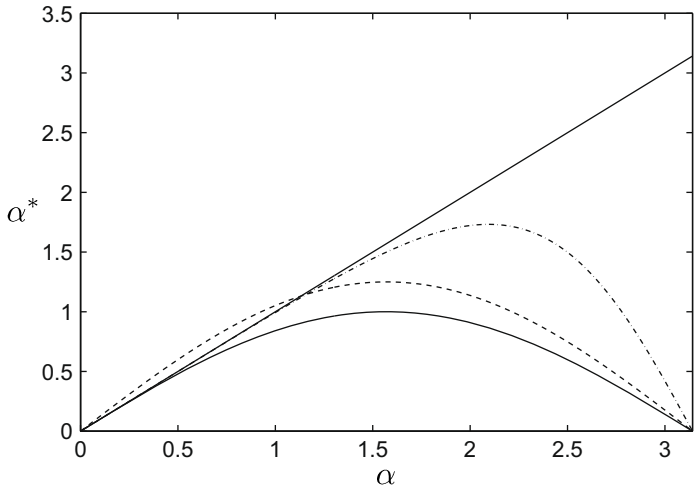

Fig. 5. Modified wavenumber of convection interpolation operators: (—) LO-CD operator, (– – –) HO-CD operator, (–·–) 4th order compact operator; the thick solid line shows the ideal profile $\alpha^* = \alpha$.

in the present code, which is defined by setting the local extrema as $\phi_{max} = \max(\phi_{nb}, \phi_0)$ and $\phi_{min} = \min(\phi_{nb}, \phi_0)$, where ϕ_{nb} denotes the scalar value at all neighboring centroids of the cell c_0. For each cell face the limiter is then computed as follows:

$$\alpha^f = \begin{cases} \min\left(1, \frac{\phi_{max}-\phi_0}{\phi_f-\phi_0}\right) & \text{if } (\phi_f - \phi_0) > 0, \\ \min\left(1, \frac{\phi_{min}-\phi_0}{\phi_f-\phi_0}\right) & \text{if } (\phi_f - \phi_0) < 0, \\ 1 & \text{otherwise}, \end{cases} \tag{21}$$

where ϕ_f is the reconstructed value at the face centroid employing the unlimited gradient. The limited gradient is finally found by setting $\alpha = \min(\alpha^f)$.

2.2. Diffusive flux reconstruction

The diffusive flux at the right-hand side of Eq. (3) is evaluated as follows:

$$\Gamma \frac{\partial \phi}{\partial x_j} A_j = \Gamma \frac{\phi_1 - \phi_0}{\Delta s} \frac{A_j A_j}{A_i s_i} - D_s, \tag{22}$$

where Δs is the distance between the neighboring cell centroids and s_i is the distance unit vector directed from the cell c_0 to the cell c_1. Note that for sake of brevity the time-level has been dropped here. The first term in Eq. (22) represents the diffusive flux along the line connecting the cell-centroids, also called *primary* diffusion. A correction term for the *secondary* or *cross* diffusion D_s is then introduced to account for the departure from grid orthogonality (i.e. whenever A_i and s_i are not aligned). In the case of unstructured grids, early attempts in the evaluation of secondary diffusion were based on the reconstruction of the scalar gradient at the cell face using interpolated node values [3,23,24]. While easy to implement in two-dimensions, the extension of this type of scheme to three-dimensional models is not straightforward. Therefore, in the present solver secondary diffusion is estimated on a cell-centered basis following the method proposed by Mathur and Murthy [25]

$$D_s = \Gamma \left[\overline{\frac{\partial \phi}{\partial x_j}} A_j - \overline{\frac{\partial \phi}{\partial x_j}} s_j \frac{A_i A_i}{A_i s_i} \right], \tag{23}$$

where the overbar denotes the arithmetic average of cell-centered values from neighboring cells. Eq. (23) shows that in this method the face scalar gradient is obtained from the average value of cell-centered gradients reconstructed from the current available solution. Using this approximation, the secondary diffusion is then evaluated at the cell-face as the difference between the diffusive flux in the face normal direction and the flux along the line connecting the cell centroids.

3. Numerical experiments

The present numerical technique is initially evaluated through the analysis of basic scalar transport problems. In the following numerical experiments the two-dimensional scalar transport equation is solved over a rectangular domain where the flow field is assumed to be known *a priori*. The basic properties of the LO-CD and HO-CD operators are in first place examined using a regular quadrilateral grid. A further comparative study is then performed over a triangular grid which is obtained by splitting each quadrilateral cell into eight right-angled triangles, as shown in Fig. 6. Using this particular grid topology, previously adopted in the work of Kim and Choi [3] and Hubbard [26], it is possible to keep an approximately constant displacement between the face centroid and the midpoint of the line connecting the center of neighboring cells (see Fig. 2). Therefore,

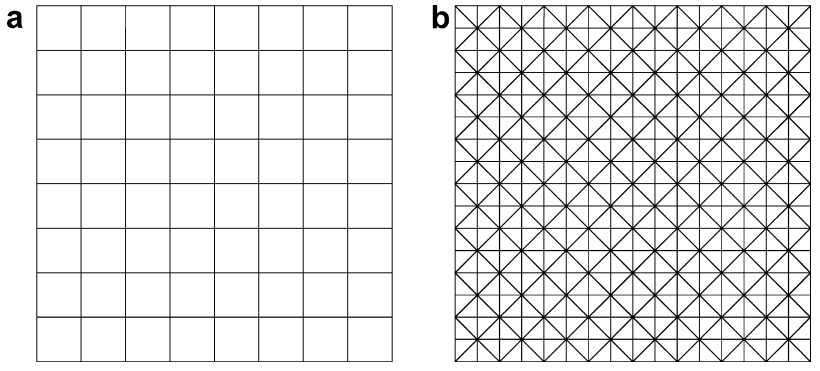

Fig. 6. Computational grids for basic numerical experiments: (a) regular quadrilateral; (b) right-angled triangular.

it is adopted in the numerical experiments to mimic and investigate the effect of arbitrary grids on the accuracy of convection interpolation operators.

3.1. Scalar transport in Taylor–Green vortex flow

The accuracy of the low and high-order central interpolation schemes is evaluated by computing the passive scalar transport in a Taylor–Green vortex flow. The analytical solution of flow governing equations is given by

$$u = -\cos(x)\sin(y)e^{-\frac{2}{Pe}t}, \tag{24}$$

$$v = \cos(y)\sin(x)e^{-\frac{2}{Pe}t}, \tag{25}$$

$$\phi = -\cos(x)\sin(y)e^{-\frac{2}{Pe}t}, \tag{26}$$

where the same momentum and scalar diffusivity is assumed and $Pe = uL/\Gamma$ is the flow Péclet number. The computational domain is $[0, 2\pi] \times [0, 2\pi]$ and periodic conditions are applied at the boundaries. The exact mass flow rate at cell faces given

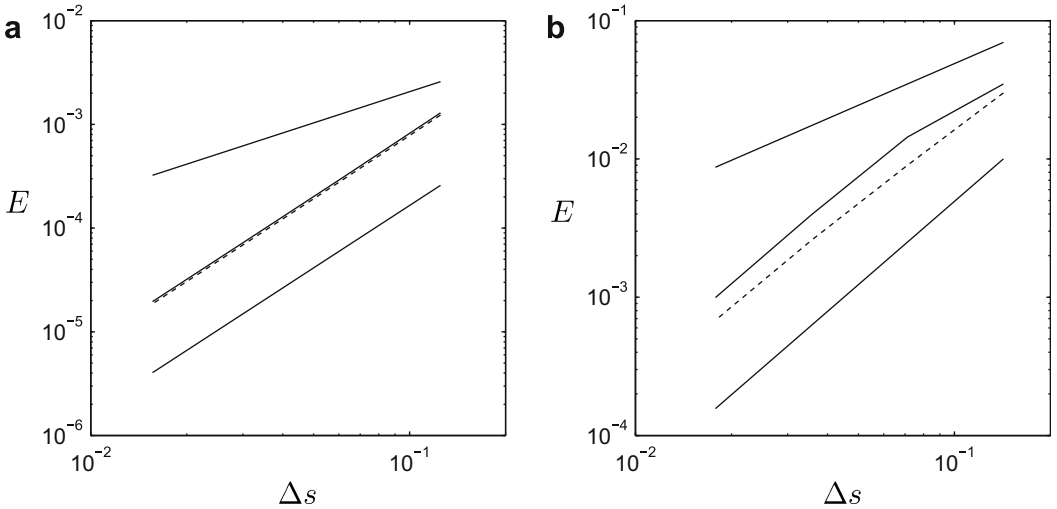

Fig. 7. Convergence history of error rms for the scalar transport in a Taylor–Green vortex flow at $Pe = 10$: (a) quadrilateral grid; (b) triangular grid; (—) LO-CD operator, (– – –) HO-CD operator; thick solid lines show ideal 1st and 2nd order slope.

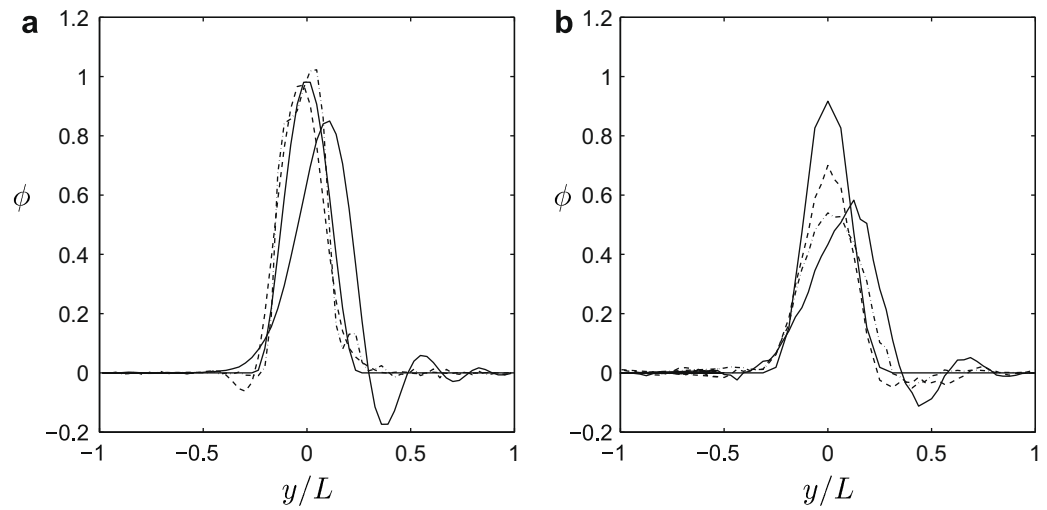

Fig. 8. Cross-sectional plot of the scalar profile after one complete revolution: (a) quadrilateral grid; (b) triangular grid; (—) LO-CD operator, (– – –) unlimited HO-CD operator, (–·–) limited HO-CD operator; the thick solid line show the initial exact profile.

by Eqs. (24) and (25) is employed in the discrete scalar transport equation, which is integrated in time starting from the initial condition obtained by setting $t = 0$ in Eq. (26). The grid refinement study is performed for a mesh spacing $\Delta s/L$ ranging from 0.25 to 0.03125, where Δs is the average distance between cell-centroids and L denotes the domain half-width.

The convergence history of the root mean square of the error between the numerical solution and the exact solution (26) is shown in Figs. 7(a) and (b) for the quadrilateral and triangular grid, respectively. As expected, both interpolation operators achieve second-order accuracy over regular quadrilateral grids, while the high-order correction term gives a significant improvement on the absolute error for the triangular grid. However, the accuracy of the LO-CD scheme is found reduced toward a first-order slope only for the largest grid-size adopted in the computations, while a second-order slope is approached for asymptotically refined grids. It is interesting to note that this result is in contrast with the findings of Kim and Choi [3] for the same type of problem, where the momentum equation has been found affected by the right-angled topology of the grid when a larger number of cells were adopted.

3.2. Scalar advection

The circular advection of a scalar profile is considered in this experiment to investigate the spectral-characteristics of interpolation schemes. The initial scalar profile is given by

Table 1
Computational setup.

Grid	L	H	W	Size	Δx^+	Δy^+	Δz^+
Coarse	$4\pi h$	$2h$	$2\pi h$	$96 \times 64 \times 80$	24	0.07–13.5	14
Fine	$4\pi h$	$2h$	$2\pi h$	$192 \times 128 \times 160$	12	0.07–5	7

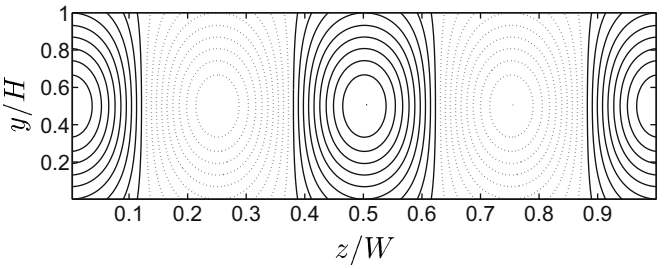

Fig. 9. Contours of the forcing function (32) in the streamwise-oriented plane $x/L = 0.5$: (—) positive values, (– – –) negative values.

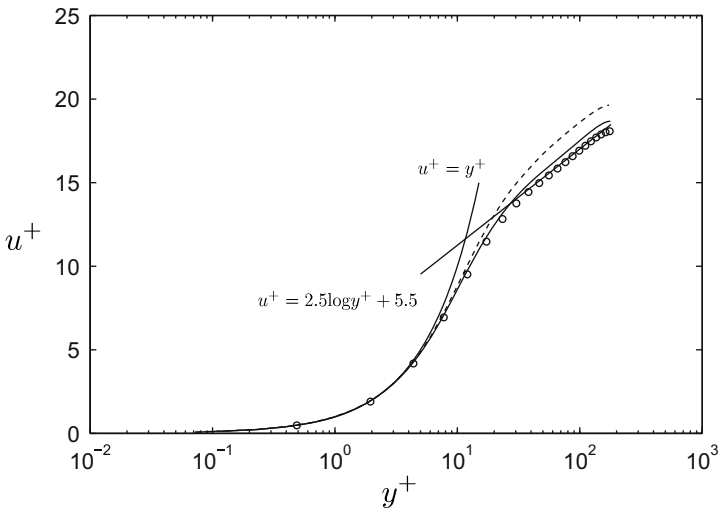

Fig. 10. Profiles of mean streamwise velocity: (– – –) coarse grid, (—) fine grid, (○) Kim et al. [31]; the thin solid line shows the law of the wall.

$$\phi = \begin{cases} \cos^2(2\pi r) & \text{if} \quad r \leqslant 0.25, \\ 0 & \text{otherwise}, \end{cases} \tag{27}$$

where $r^2 = (x + 0.5)^2 + y^2$. The computational domain is $[-1, 1] \times [-1, 1]$ and a null scalar value is assigned at the boundaries. The profile is advected by the velocity field $u_j \equiv (-2\pi y, 2\pi x)$ and it should return unchanged to its original position after a complete revolution. Note that both the unlimited and the limited high-order scheme are employed to examine the interaction between the adopted slope-limiter technique and the spectral properties of interpolation operators. A fixed grid spacing $\Delta s/L$ of 0.03125 is employed in the computations, where L denotes again the domain half-width.

The computed scalar profiles after one rotation are shown in Fig. 8. The results obtained for the regular quadrilateral grid are consistent with the Fourier analysis presented in Section 2. The unlimited HO-CD operator gives a significant reduction of numerical dispersion compared to the LO-CD scheme, which is characterized by severe oscillations in the upwind region of the predicted profile. It is also worth noting that wiggles travel faster in the case of the high-order operator, in agreement with the faster numerical phase speed highlighted by the modified wavenumber profile in Fig. 5. On the contrary, the profile given by the LO-CD schemes is shifted toward higher y/L due to the lower numerical phase speed compared to the exact profile, as shown in Fig. 5. The slope-limiter technique is found able to avoid the undershoot at the downwind side of the profile given by the unlimited high-order scheme. However, it is also characterized by high-frequency modes indicating a

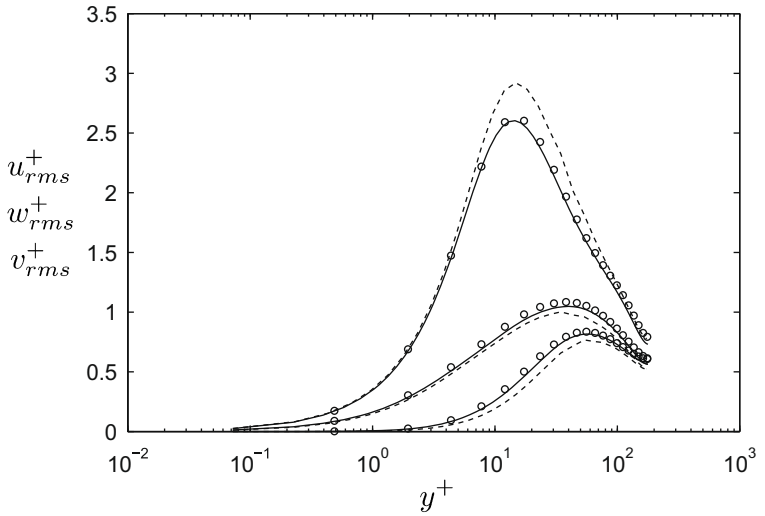

Fig. 11. Profiles of root mean square of velocity fluctuations: (– – –) coarse grid, (—) fine grid, (○) Kim et al. [31].

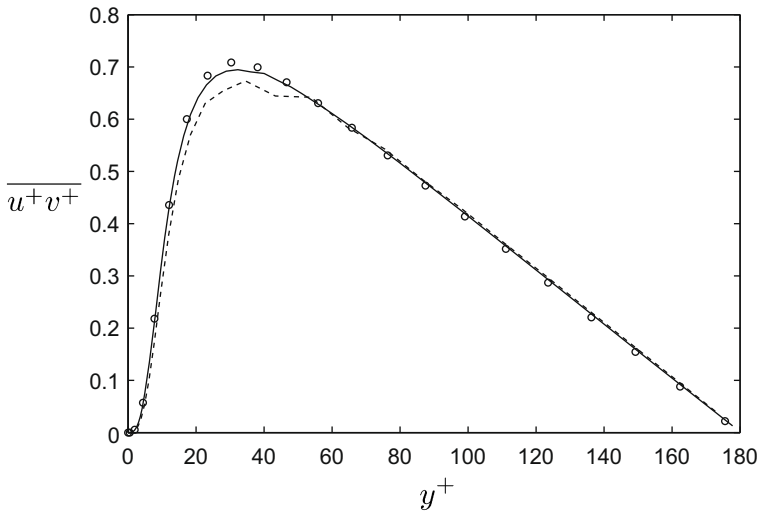

Fig. 12. Profiles of Reynolds stress: (– – –) coarse grid, (—) fine grid, (○) Kim et al. [31].

stronger dispersive character resulting from the action of the slope-limiter. The profile peak is finally found clearly improved by the unlimited and limited HO-CD operator compared to the LO-CD scheme. A significant improvement is also obtained over the triangular grid when the unlimited high-order scheme is employed, while the limited operator gives a similar pre-

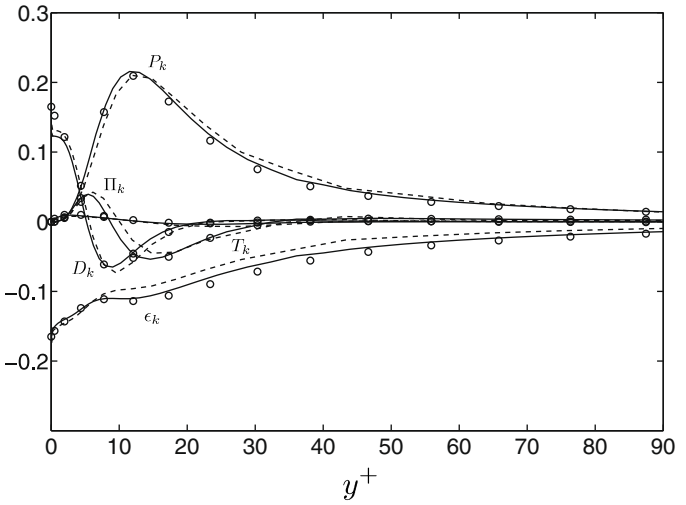

Fig. 13. Individual contributions to the turbulent kinetic energy balance in wall units: (P_k) production, (T_k) turbulent mixing, (Π_k) pressure diffusion, (D_k) viscous diffusion, (ϵ_k) dissipation; (– – –) coarse grid, (—) fine grid, (○) Kim et al. [31].

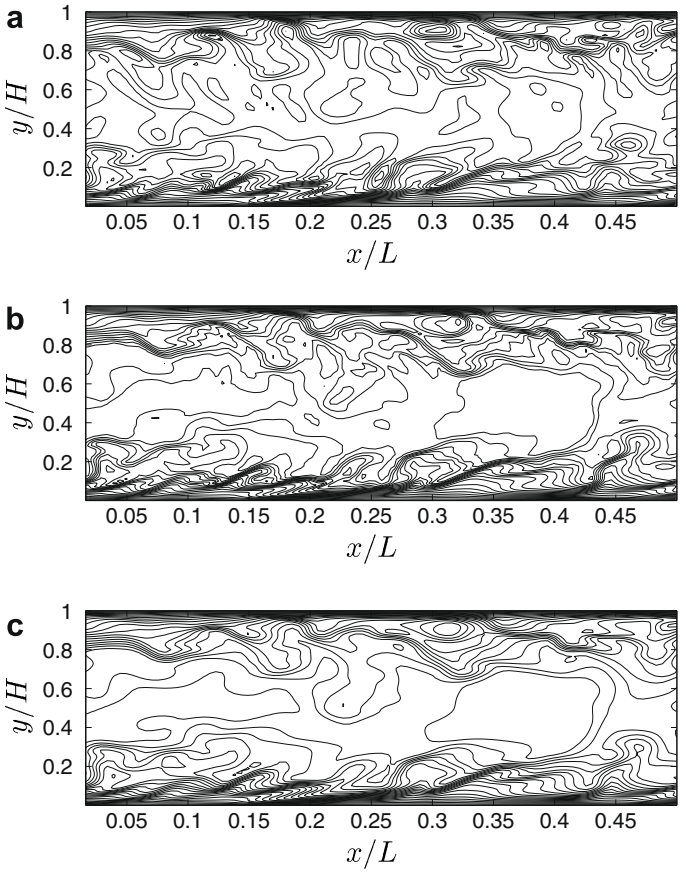

Fig. 14. Instantaneous scalar field in the spanwise-oriented section $z/W = 0.5$, (a) LO-CD operator, (b) HO-CD operator, (c) SOU operator.

diction of the maximum value compared to the low-order interpolation. However, both high-resolution schemes show reduced dispersion characteristics at the upwind side of the profile.

4. Direct numerical simulations

In this section the scalar transport in a turbulent flow within a flat channel is investigated using direct numerical simulations. The analysis is performed to validate the code against the database of Kasagi et al. [27], which has been established through an accurate pseudo-spectral technique [28]. Furthermore, it provides a more challenging test case for the comparative study of convection interpolation operators. An incompressible Newtonian fluid with constant properties is assumed in the computations. The flow governing equations thus read as follows:

$$\frac{\partial u_i}{\partial x_i} = 0, \tag{28}$$

$$\frac{\partial u_i}{\partial t} + \frac{\partial (u_j u_i)}{\partial x_j} = -\frac{1}{\rho}\frac{\partial p}{\partial x_i} + \nu \frac{\partial^2 u_i}{\partial x_j \partial x_j}, \tag{29}$$

$$\frac{\partial \phi}{\partial t} + \frac{\partial (u_j \phi)}{\partial x_j} = D \frac{\partial^2 \phi}{\partial x_j \partial x_j} + S, \tag{30}$$

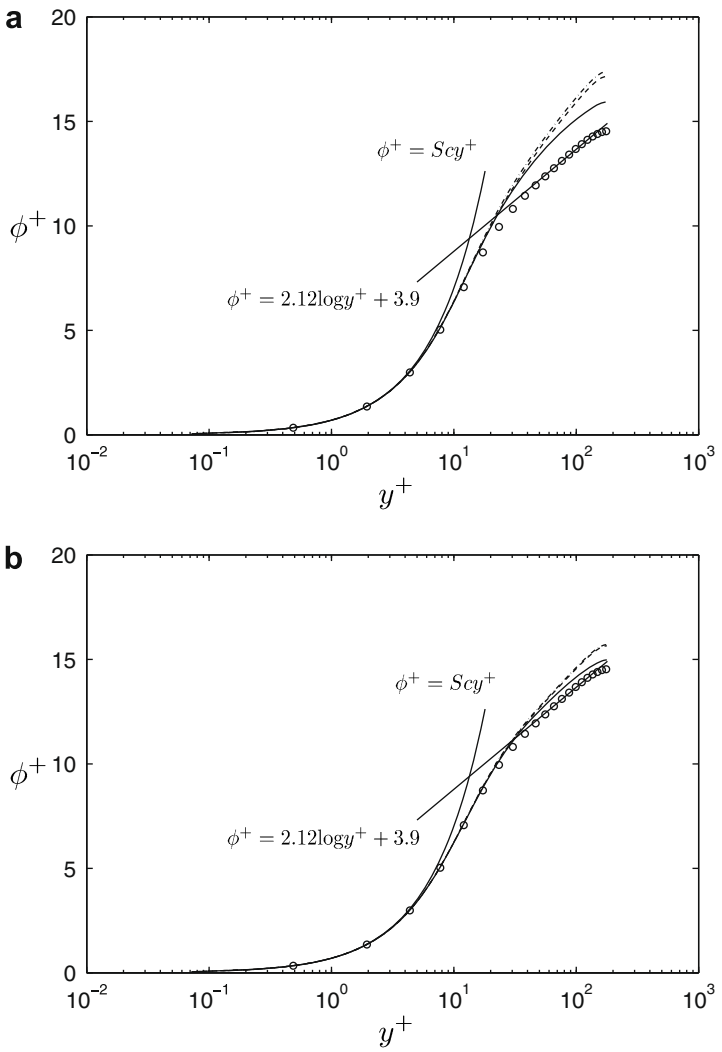

Fig. 15. Mean scalar profiles: (a) coarse grid, (b) fine grid; (–·–) SOU operator, (– – –) HO-CD operator, (—) LO-CD operator, (○) Kasagi et al. [27]; the thin solid line shows Kader's empirical formula [32].

where Eqs. (28) and (29) are the Navier–Stokes equations, Eq. (30) is the scalar transport equation and D denotes the scalar diffusivity. The scalar transport is approximated as a *passive* mechanism, thus the momentum and the scalar transport equations are decoupled and they can be solved in a segregated manner. The flow governing Eqs. (28) and (29) are solved with the help of the finite-volume code FLUENT. The pressure–velocity coupling is performed by the Fractional Step method [29] and the LO-CD operator is adopted for the discretization of advective terms. Note that a comparative study of the LO-CD operator, a distance-weighted central interpolation and a third-order upwind biased scheme for the momentum equation has been recently presented in the framework of finite-volume schemes by Felten and Lund [6] using LES for a similar flow and grid configuration, showing that the low-order scheme gives reliable predictions of the velocity field. Therefore, the same type of analysis has not been considered here. Once the velocity field is obtained, the available mass flow rates are employed to evaluate the advective transport term of the scalar Eq. (30). Note that the FLUENT code is based on the co-located arrangement of pressure and velocity. Therefore, the mass flow rates are corrected using the momentum interpolation technique of Rhie and Chow [7] in order to satisfy the continuity constraint.

The channel is composed of two flat plates and the flow is assumed fully developed and driven by a constant pressure gradient. The streamwise (x-wise) and spanwise (z-wise) directions are both homogeneous and therefore periodic boundary conditions are applied. The passive scalar is uniformly generated within the fluid by the source term at right-hand side of Eq. (30) and then removed at the walls, where a constant scalar value is specified. The flow Reynolds number is $Re_\tau = 180$, based on the channel half-width h and the friction velocity u_τ, while the adopted fluid Schmidt number $Sc = \nu/D$ is 0.7. An orthogonal finite-volume grid consisting of hexahedral cells is employed in the analysis. Uniform grid spacing is adopted along both the streamwise and spanwise directions, while the grid is hyperbolically stretched toward the solid surfaces. The extent of

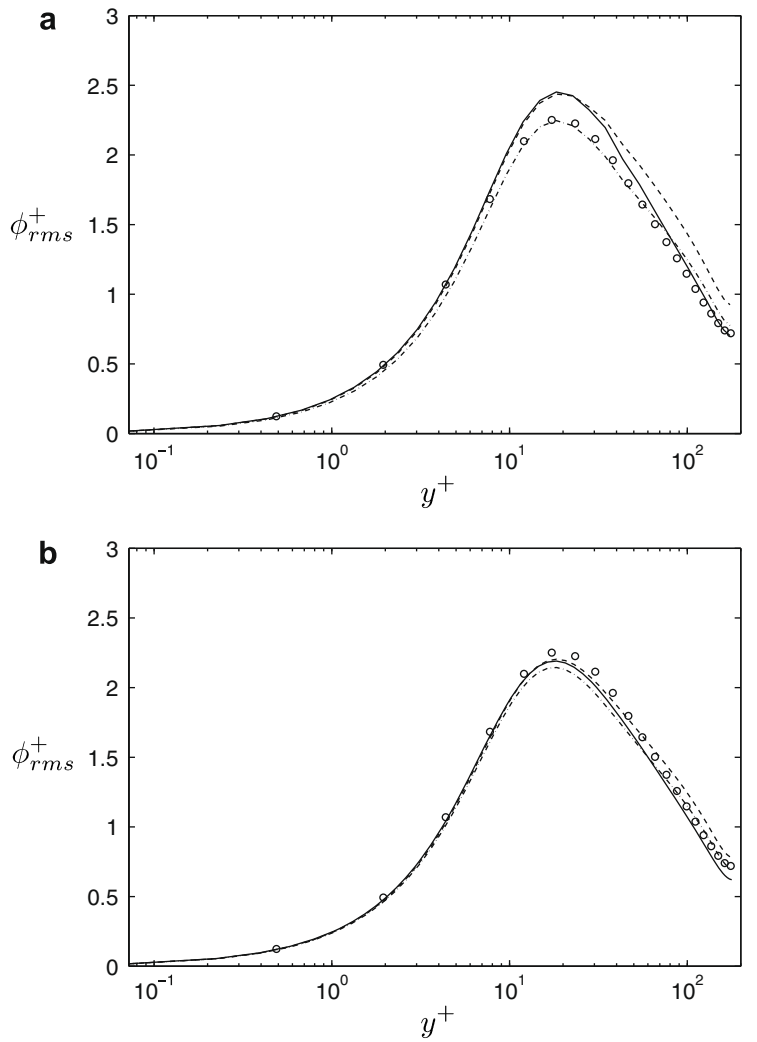

Fig. 16. Profiles of root mean square of scalar fluctuations: (a) coarse grid, (b) fine grid; (– · –) SOU operator, (– – –) HO-CD operator, (–) LO-CD operator, (○) Kasagi et al. [27].

the computational domain and the grid resolution normalized by wall units are reported in Table 1. It is worth noting that the finest grid resolution is of the same order of the reference dataset [27].

The initial flow conditions are defined as follows:

$$\begin{aligned} u(x,y,z,0) &= u_L, \\ v(x,y,z,0) &= F, \\ w(x,y,z,0) &= 0, \end{aligned} \tag{31}$$

where u_L is a laminar velocity profile for fully developed conditions at the same flow Reynolds number. In order to promote the transition to fully developed turbulence, a spatially decaying disturbance [30] centred at the channel center $(x_{\mathrm{loc}} = L/2, y_{\mathrm{loc}} = H/2)$ is then introduced on the vertical velocity component

$$F = C \exp[-((x - x_{\mathrm{loc}})/x_{\mathrm{scale}})^2] \exp[-((y - y_{\mathrm{loc}})/y_{\mathrm{scale}})^2] g(z), \tag{32}$$

where the constant C controls the strength of the disturbance and $x_{\mathrm{scale}}, y_{\mathrm{scale}}$ give the spatial extent. The spanwise frequency of the forcing is controlled by $g(z) = cos(\beta z)$. A value of $\beta = 4$ is employed in the present computations, which gives the contours of the forcing function shown in Fig. 9. The initial condition for the scalar field is finally obtained by setting

$$\phi(x,y,z,0) = Sc|u|. \tag{33}$$

The time-integration of governing equations is started with the largest admissible time step size for numerical stability until an approximate statistically steady-state is reached. At this point, the time step size is reduced to $3.7 \times 10^{-4} \Delta t u_\tau / h$ and sta-

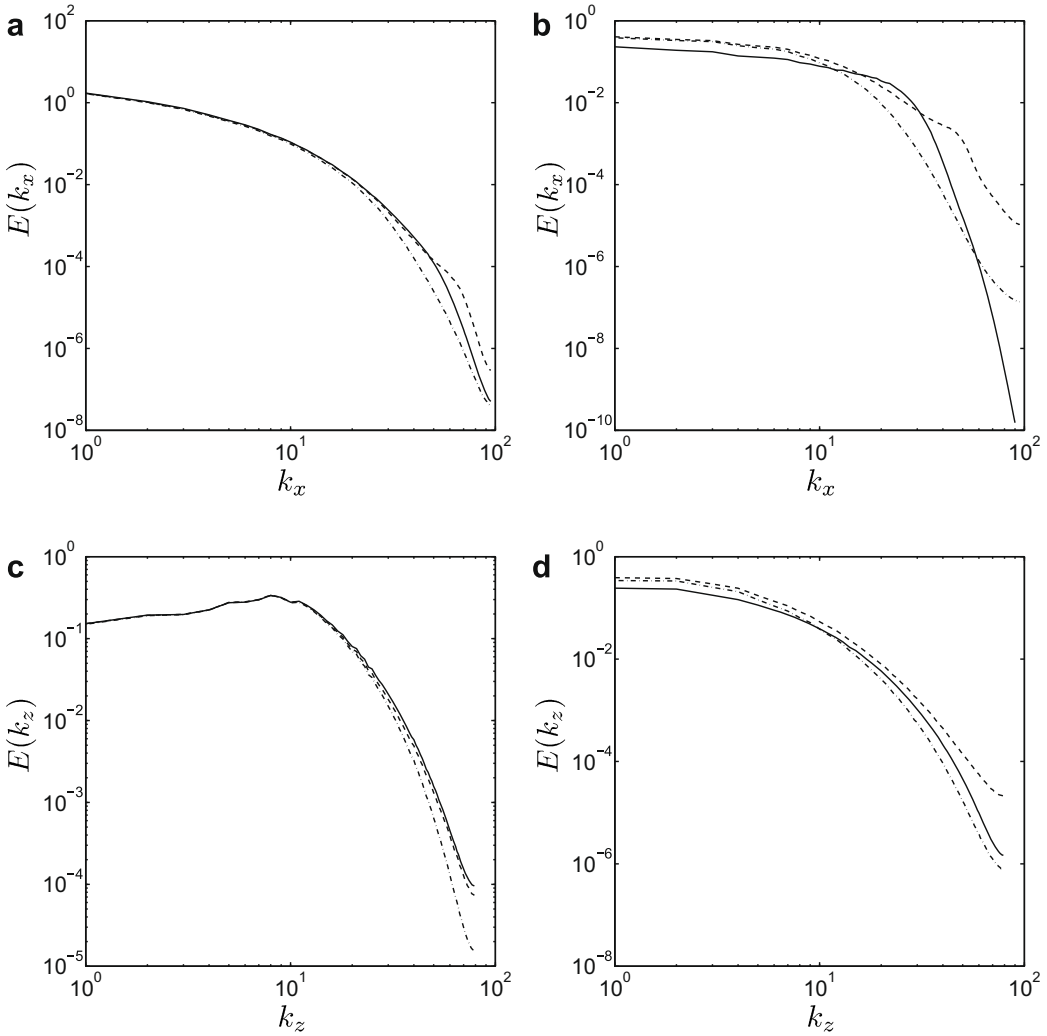

Fig. 17. One-dimensional spectra of scalar fluctuations for the fine grid: (a) streamwise spectrum at $y^+ \approx 5$, (b) streamwise spectrum at $y^+ \approx 149$, (c) spanwise spectrum at $y^+ \approx 5$, (d) spanwise spectrum at $y^+ \approx 149$; (–·–) SOU operator, (– – –) HO-CD operator, (—) LO-CD operator.

tistical samples are collected over a period of approximately 25 viscous time units. Spatial averaging is also performed along the homogeneous directions in order to improve the convergence of time-averaged statistics.

In order to establish if reliable mass fluxes are provided to the scalar transport equation, the flow field results are compared to the numerical dataset of Kim et al. [31]. Note that the finest grid resolution reported in Table 1 is also in this case of the same order of the reference dataset. Mean velocity profiles are compared in Fig. 10. The agreement with the spectral code and the law of the wall for the finest grid is excellent in the viscous sublayer ($y^+ \leqslant 5$) and in the buffer layer ($5 \leqslant y^+ \leqslant 30$), while in the logarithmic and outer regions ($y^+ \geqslant 30$) the present profile falls slightly above the reference data. It is also interesting to note that in the log-region the coarse grid gives a reliable prediction of the profile slope, but significantly exceeds the constant term in the law of the wall. The root mean square of velocity fluctuations is presented in Fig. 11. As expected, each of the three velocity components significantly benefits from the grid refinement. The improvement is largely felt by the streamwise and spanwise velocity in the log-region and in the outer layer, while the vertical component is also strongly affected within the buffer layer. However, while most streamwise fluctuations are well-captured throughout the channel, both the vertical and spanwise components are slightly understimated between the wall and the buffer layer ($y^+ < 30$) even when the finest grid is employed. The analysis of Reynolds stress profiles in Fig. 12 suggests that the overpredicted constant term of the mean velocity profile in the range $y^+ \geqslant 30$ is determined by the slightly understimated stress level in the same region. This is also confirmed by the coarse grid profile, which significantly falls below the reference dataset. Both profiles show a good agreement for $y^+ > 60$ while the buffer layer is strongly influenced by the grid resolution. The turbulent kinetic energy balance is finally evaluated in Fig. 13 to establish if the individual contributions are properly predicted by the numerical technique. The computed profiles give an overall good agreement with the spectral dataset, since both the magnitude and locations of local maxima are correctly reproduced when the finest grid resolution is employed. The comparative anal-

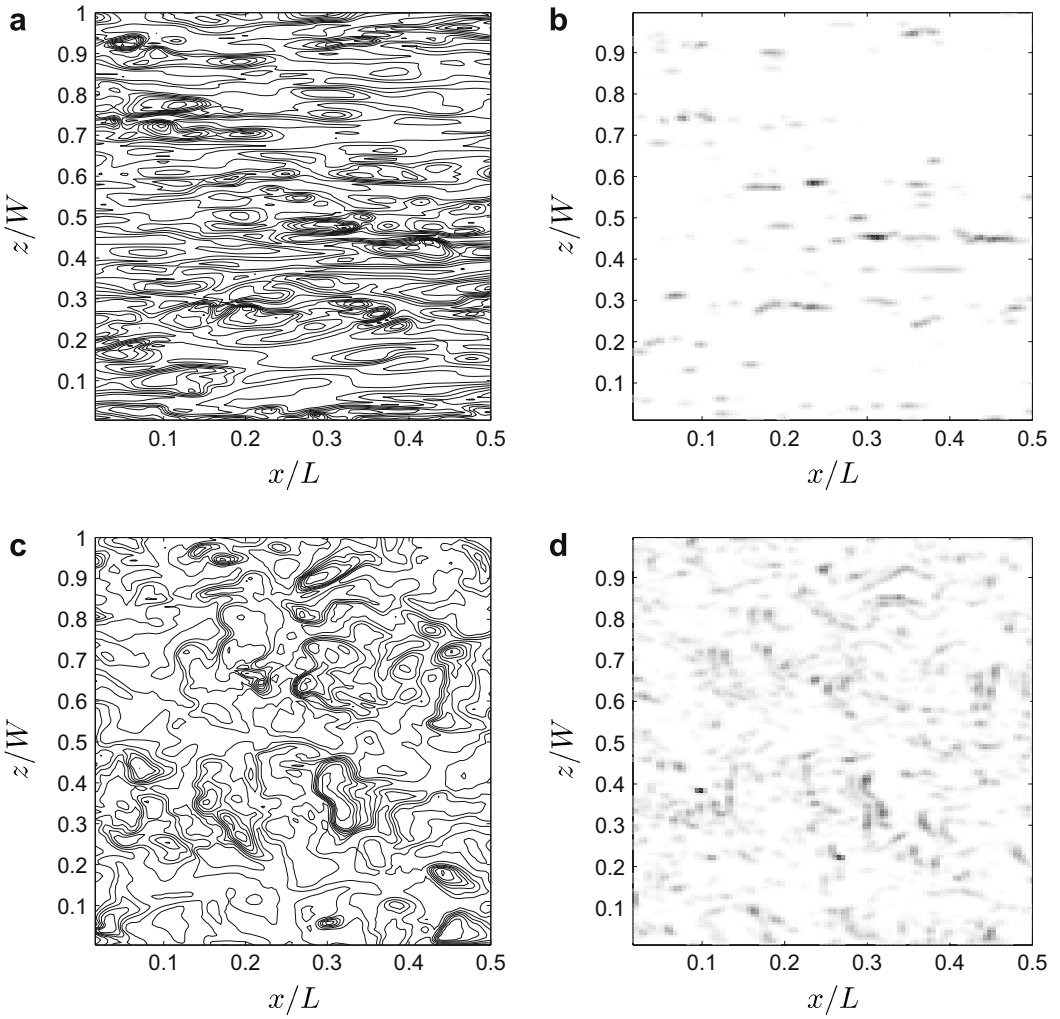

Fig. 18. Instantaneous scalar field (left column) and associated slope-limiter magnitude (right column) in vertical-oriented sections: (a) and (b) $y^+ \approx 5$, (c) and (d) $y^+ \approx 149$; the slope-limiter magnitude ranges from 0 (white) to 1 (black).

ysis with the results obtained with the coarse grid highlights noticeable changes in turbulent mixing, viscous diffusion and dissipation profiles while the production term and the pressure diffusion are found substantially unaffected by the grid resolution.

The computed statistics for the flow field show that reliable predictions of both the mean field and second-order moments is obtained by the solution of the flow governing Eqs. (28), (29) using the FLUENT code. Therefore, available mass flow rates at cell faces are employed in the present code to solve the scalar transport Eq. (30) using the LO-CD and the limited HO-CD operators. Note that a limited second-order upwind scheme (SOU) is further adopted in the analysis as a reference upwind-biased interpolation. A picture of the instantaneous scalar field is presented in Fig. 14. As it can be noted, none of the contours plot show evidence of numerical wiggles, thus indicating that deferred-correction and slope-limiter techniques lead to stable solutions also when central interpolations operators are employed for the scalar transport equation. However, while the structure of the scalar field is found fairly similar close to the wall, the contour levels in the channel core highlight a broader range of lengthscales predicted by the LO-CD and HO-CD schemes compared to the SOU operator.

Mean scalar profiles are shown in Fig. 15. Unexpectedly, the HO-CD and SOU operators yield the same overpredicted profile slope in the log-region, which is clearly in poor agreement with both the spectral dataset and the empirical formula of Kader [32]. Although a slight improvement is given by the high-resolution scheme over the upwind-biased interpolation on the coarse mesh, it is clear that only the LO-CD scheme is able to give a reliable prediction of the profile slope for both grids.

In spite of the similar results obtained for the mean field, the profiles of scalar variance in Fig. 16 clearly show a different interaction of interpolation operators with turbulent fluctuations. Up to the buffer layer ($y^+ \leqslant 30$) the profile predicted by the high-order central scheme overlaps the profile given by the low-order central operator. In the same range the SOU

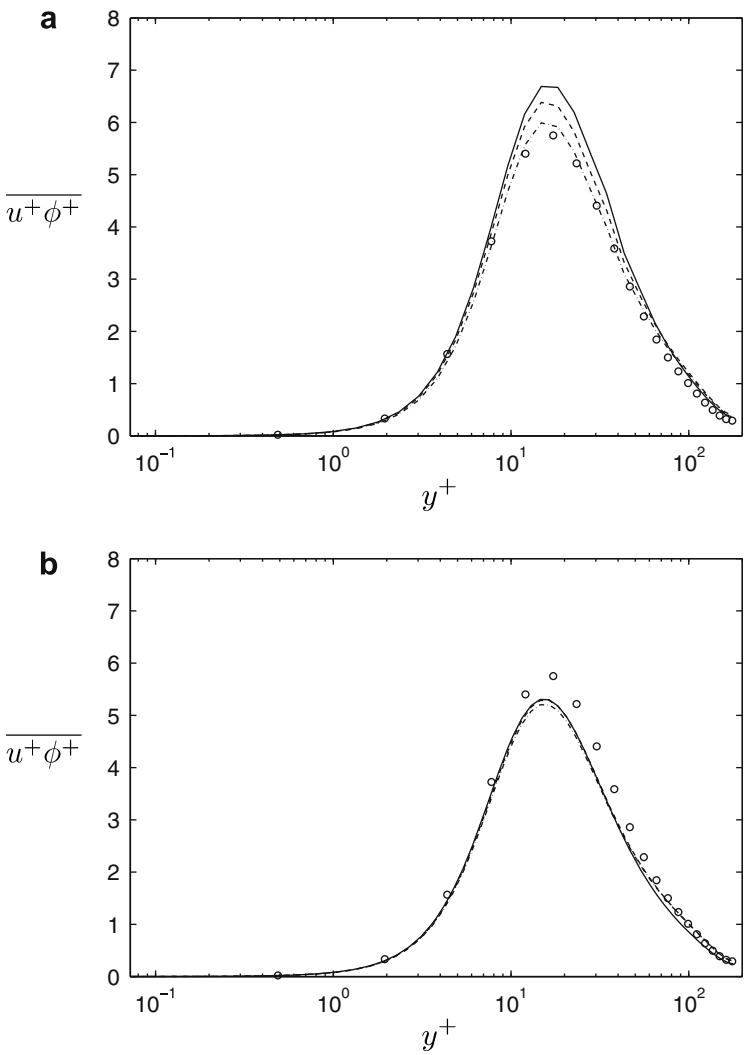

Fig. 19. Profiles of streamwise turbulent scalar flux: (a) coarse grid; (b) fine grid; (–·–) SOU operator, (– – –) HO-CD operator, (—) LO-CD operator, (○) Kasagi et al. [27].

scheme yields a significant reduction of scalar fluctuations on the coarse grid, indicating a stronger dissipative character for the upwind-biased interpolation. This is also confirmed by the results for the fine grid, where the maximum value given by the SOU operator is clearly underestimated compared to both central schemes. In the log-region and in the outer layer ($y^+ \geqslant 30$) the scalar variance is largely overpredicted by the HO-CD scheme. It is worth noting that the same result has been reported by Châtelain et al. [15] for a fourth-order central scheme accounting for the mesh stretching. However, in the present computations a similar scenario is also found in the case of the upwind-biased operator. On the contrary, the low-order central scheme gives a good agreement with the spectral dataset within the whole channel height.

In order to give further insight on spectral-characteristics of adopted interpolation operators, one-dimensional spectra of scalar fluctuations are presented in Fig. 17. The computed spectrum within the viscous sublayer ($y^+ \approx 5$) in Fig. 17(a) and (c) shows a reduced energy-content over the upper-half range of wavenumbers along both the streamwise and spanwise directions for the SOU operator, which is clearly associated with the dissipative nature of the numerical error. On the contrary the computed spectrum of central interpolation operators compares fairly well in the spanwise direction, while the high-resolution scheme gives rise to a pile-up of energy-content in the streamwise spectrum at the highest wavenumbers. Although this scenario is in contrast with the improved spectral resolution of the HO-CD operator resulting from the Fourier analysis presented in Section 2, the energy pile-up suggests a stronger dispersive nature of the numerical error associated with asymmetric interpolations given by the high-resolution scheme when employed over arbitrary grids. A similar picture is found for the spanwise spectrum in the outer layer ($y^+ \approx 149$) shown in Fig. 17(d), where in the dissipative wavenumber range the high-order central and the upwind-biased scheme yield a reduced and stronger energy-content, respectively. However, in

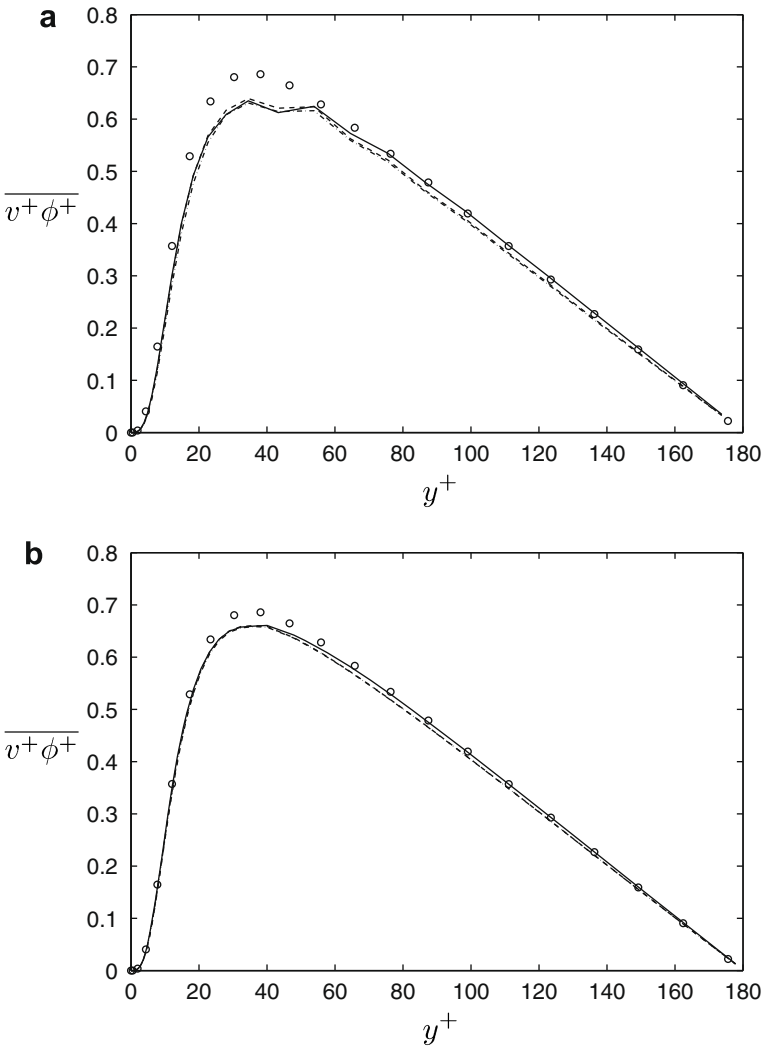

Fig. 20. Profiles of vertical turbulent scalar flux: (a) coarse grid; (b) fine grid; (–·–) SOU operator, (– – –) HO-CD operator, (—) LO-CD operator, (○) Kasagi et al. [27].

this case the high-order scheme is also characterized by a flat tail in the energy spectrum which is not found in the viscous sublayer. From the analysis of the streamwise spectrum in Fig. 17(b) it can be noted that the same effect is present in the high-order central and upwind-biased profiles. It is finally interesting to note that in the outer layer the HO-CD and SOU operators yield the same overpredicted energy-content compared to the LO-CD spectrum in the first-half of the wavenumbers range.

The significant changes in computed one-dimensional spectra for the HO-CD scheme within the viscous and the outer layer can be partly explained through the analysis of the instantaneous scalar field and the associated slope-limiter magnitude in Fig. 18. The structure of the scalar field in the viscous sublayer shown in Fig. 18(a) is characterized by streamwise-elongated patches having a nearly constant scalar value. Therefore, the action of the slope-limiter is confined to the edges of these structures and fully-limiting conditions are limited to a small amount of cells. However, in the outer-layer fully developed turbulent structures depicted in Fig. 18(c) give rise to sharp gradients in the scalar field and the action of the slope-limiter in Fig. 18(d) is found to be clearly stronger. It can then be concluded that the tail of the one-dimensional spectrum for the HO-CD operator in Fig. 17(b) is affected by the interaction of the adopted slope-limiter technique and the dissipative range of turbulent length-scales. Moreover, note that Ikeda & Durbin [33] have also reported a significant effect on high-wavenumber modes when mesh stretching is accounted for by interpolation operators.

The profiles of turbulent scalar fluxes are finally examined in Figs. 19 and 20. Although the streamwise component is found clearly underpredicted by each intepolation operator when the fine grid is employed, both the low and high-order central schemes yield a slight improvement of computed profiles in the range $0 \leqslant y^+ \leqslant 30$. The predicted maximum value of the vertical component in Fig. 20 is found to be closer to the spectral dataset and apparently independent from adopted interpolation schemes, but the turbulent flux is found to be underpredicted by the HO-CD and the SOU operators in the range $50 \leqslant y^+ \leqslant 180$.

5. Conclusions

An unstructured finite-volume scheme for high-fidelity simulations of scalar transport in complex geometries has been presented and investigated. The analysis has been focused to a preliminary study aimed at establishing a suitable interpolation operator for the advective term of the scalar transport equation over arbitrary grids. In this framework, a symmetric low-order central scheme and a high-order central operator adopting a correction term based on cell-centered gradients have been employed and compared for scalar reconstruction at cell faces. In order to improve the numerical stability of the numerical scheme, both central operators have been introduced implicitly in the resulting discrete scalar transport equation with the help of the deferred-correction technique.

An initial evaluation of interpolation schemes performed through basic numerical experiments has shown an improved spatial-accuracy of the high-order operator in the analysis of convection–diffusion problems over arbitrary grids. However, the accuracy of the low-order operator has been found to be reduced toward a first-order slope only for the largest grid size adopted in the computations. The analysis of a two-dimensional scalar advection problem has also proved the higher spectral-resolution of the high-order scheme compared to the standard symmetric operator, in agreement with the transfer function and modified wavenumber profiles predicted by the Fourier analysis of truncation errors.

A direct numerical simulation of turbulent scalar transport in a channel flow has been then performed in order to provide a further comparative study of convective interpolation operators and to validate the numerical technique against a spectral dataset. In spite of the linear character of the scalar transport equation, the results have been found significantly affected by the spectral-properties of adopted interpolation schemes. The analysis of one-dimensional spectra of scalar fluctuations revealed a stronger dispersive character of the high-order interpolation resulting in an evident energy pile-up at the highest wavenumbers range. Moreover, the energy-content of the scalar spectrum has also been found to be affected by the interaction between the dissipative range of turbulent length-scales and the slope-limiter technique adopted in the high-order scheme to preserve the boundedness of interpolated face values. The resulting slope of the mean scalar profile predicted by the high-order operator in the log-region has been found to be clearly overpredicted compared to the low-order operator and the spectral dataset. It is interesting to note that the same overpredicted slope has also been given by a second-order upwind scheme adopted as a reference upwind-biased operator. Although the analysis of the root mean square of scalar fluctuations suggests that the high-resolution scheme is able to minimize the numerical dissipation given by an asymmetric interpolation, the present results have shown greater reliability for the standard low-order central operator in the analysis of scalar transport in the turbulent channel flow.

Acknowledgments

The High Performance Computing Center at Stanford University is gratefully acknowledged for providing computing resources that have contributed to the research results presented in this paper. The author would also like to thank Prof. P. Moin, Prof. G Iaccarino and Dr. Frank Ham for helpful suggestions during the preparation of the manuscript.

References

[1] P. Moin, K. Mahesh, Direct numerical simulation: a tool in turbulent research, Annu. Rev. Fluid Mech. 30 (1998) 539.

[2] K. Mahesh, G.R. Ruetsch, P. Moin, Towards large-eddy simulation in complex geometries, Annual Research Briefs, Center for Turbulence Research, Stanford University and NASA-Ames 379 (1999).
[3] D. Kim, H. Choi, A second-order time-accurate finite volume method for unsteady incompressible flow on hybrid unstructured grids, J. Comput. Phys. 162 (2000) 411.
[4] K. Mahesh, G. Constantinescu, P. Moin, A numerical method for large-eddy simulation in complex geometries, J. Comput. Phys. 197 (2004) 215.
[5] K. Mahesh, G. Constantinescu, S.V. Apte, G. Iaccarino, F. Ham, P. Moin, Progress toward large-eddy simulation of turbulent reacting and non-reacting flows in complex geometries, Annual Research Briefs, Center for Turbulence Research, Stanford University and NASA-Ames 115 (2002).
[6] F.N. Felten, T.S. Lund, Kinetic energy conservation issues associated with the collocated mesh scheme for incompressible flows, J. Comput. Phys. 215 (2006) 465.
[7] C.M. Rhie, W.L. Chow, A numerical study of the turbulent flow past an isolated airfoil with trailing edge separation, AIAA J. 21 (1983) 1525.
[8] S. Benhamadouche, K. Mahesh, G. Constantinescu, Colocated finite-volume schemes for large-eddy simulation on unstructured meshes, in: Proceedings of the Summer Program, Center for Turbulence Research, Stanford University and NASA-Ames, vol. 143, 2002.
[9] A. Silva Lopes, J.M.L.M. Palma, Numerical simulation of isotropic turbulence using a collocated approach and a nonorthogonal grid system, J. Comput. Phys. 175 (2002) 713.
[10] M. Herrmann, G. Blanquart, V. Raman, Flux corrected finite-volume scheme for preserving scalar boundedness in large-eddy simulations, Annual Research Briefs, Center for Turbulence Research, Stanford University and NASA-Ames 75 (2004).
[11] C.D. Pierce, Progress variable approach for large-eddy simulation of turbulent combustion, PhD Thesis, Stanford University, 2001.
[12] M. Piller, E. Nobile, Direct numerical simulation of turbulent heat transfer in a square duct, Int. J. Numer. Methods Heat Fluid Flow 12 (2002) 658.
[13] M. Piller, E. Nobile, T.J. Hanratty, DNS study of turbulent transport at low Prandtl numbers in a channel flow, J. Fluid Mech. 458 (2002) 419.
[14] E. Stalio, E. Nobile, Direct numerical simulation of heat transfer over riblets, Int. J. Heat Fluid Flow 24 (2003) 356.
[15] A. Châtelain, F. Ducros, O. Metais, LES of turbulent heat transfer: proper convection numerical schemes for temperature transport, Int. J. Numer. Methods Fluids 44 (2004) 1017.
[16] P. Batten, C. Lambert, D.M. Causon, Positively conservative high-resolution convection schemes for unstructured elements, Int. J. Numer. Methods Eng. 39 (1996) 1821.
[17] P.K. Khosla, S.G. Rubin, A diagonally dominant second-order accurate explicit scheme, Comput. Fluids 2 (1974) 207.
[18] J. Ferziger, M. Peric, Computational Methods for Fluid Dynamics, third ed., Springer, Berlin, 2001.
[19] H. Choi, P. Moin, J. Kim, Direct numerical simulation of turbulent flow over riblets, J. Fluid Mech. 255 (1993) 503.
[20] Y. Li, Wavenumber-extended high-order upwind biased finite-difference schemes for convective scalar transport, J. Comput. Phys. 133 (1997) 235.
[21] B. Van Leer, Towards the ultimate conservative difference scheme. V.A Second-order sequel to Godunov's method, J. Comput. Phys. 32 (1979) 101.
[22] T.J. Barth, D.C. Jespersen, The design and application of upwind schemes on unstructured meshes, AIAA Paper 89 (1989).
[23] L. Davidson, A pressure correction method for unstructured meshes with arbitrary control volumes, Int. J. Numer. Methods Fluids 22 (1996) 265.
[24] Y.G. Lai, An unstructured grid method for a pressure-based flow and heat transfer solver, Numer. Heat Transfer Part B 32 (1997) 267.
[25] S.R. Mathur, J.Y. Murthy, A pressure-based method for unstructured meshes, Numer. Heat Transfer Part B 31 (1997) 195.
[26] M.E. Hubbard, Multidimensional slope-limiters for MUSCL-Type finite volume schemes on unstructured grids, J. Comput. Phys. 155 (1999) 54.
[27] N. Kasagi, K. Horiuti, Y. Myiake, T. Miyauchi, Y. Nagano, Establishment of the direct numerical simulation data bases of turbulent transport phenomena, Co-operative Research No. 02302043, Tokyo University, 1992 .
[28] P. Moin, J. Kim, On the numerical solution of time-dependent viscous incompressible fluid flows involving solid boundaries, J. Comput. Phys. 35 (1979) 381.
[29] S.E. Kim, B. Makarov, An implicit fractional-step method for efficient transient simulations of incompressible flows, 17th AIAA Computational Fluid Dynamics Conference, Toronto, Canada, 2005.
[30] P. Andersson, L. Brandt, A. Bottaro, D.S. Henningson, On the breakdown of boundary layer streaks, J. Fluid Mech. 428 (2001) 29.
[31] J. Kim, P. Moin, R. Moser, Turbulence statistics in fully developed channel flow at low Reynolds number, J. Fluid Mech. 177 (1987) 133.
[32] B.A. Kader, Temperature and concentration profiles in fully developed turbulent boundary layers, Int. J. Heat Mass Transfer 24 (1981) 1541.
[33] T. Ikeda, P.A. Durbin, Mesh stretch effects on convection in flow simulations, J. Comput. Phys. 199 (2004) 110.